Limits on neutrino oscillations from $\bar{\nu}_e$ appearance

S. J. Freedman,* B. K. Fujikawa,* J. Napolitano,† and J. E. Nelson
Argonne National Laboratory, Argonne, Illinois 60439

R. D. McKeown
California Institute of Technology, Pasadena, California 91125

K. T. Lesko
Lawrence Berkeley Laboratory, Berkeley, California 94720

J. B. Donahue, G. T. Garvey, and V. D. Sandberg
Los Alamos National Laboratory, Los Alamos, New Mexico 87545

W. C. Choi,‡ A. Fazely,§ R. L. Imlay, and W. J. Metcalf
Louisiana State University, Baton Rouge, Louisiana 70803

L. S. Durkin, R. W. Harper,** T. Y. Ling, J. W. Mitchell,†† T. A. Romanowski,
E. S. Smith,†† and M. Timko§§
The Ohio State University, Columbus Ohio 43210
(Received 22 July 1992)

A 20-ton neutrino detector located near the Los Alamos Meson Physics Facility beam stop is used to search for $\bar{\nu}_e$ generated via neutrino oscillations from any of the three neutrino types, ν_μ, $\bar{\nu}_\mu$, and ν_e, which radiate from the beam stop. The analysis of three years of data provides limits on the oscillation modes $\bar{\nu}_\mu \rightarrow \bar{\nu}_e$, $\nu_e \rightarrow \bar{\nu}_e$, and $\nu_\mu \rightarrow \bar{\nu}_e$, and the lepton-number-violating decay process $\mu^+ \rightarrow e^+ + \bar{\nu}_e + \nu_\mu$. The 90%-confidence-level limits for $\bar{\nu}_\mu \rightarrow \bar{\nu}_e$ oscillations are $\delta m^2 \leq 0.14$ eV^2 for maximal mixing, and $\sin^2 2\theta \leq 0.024$ for large δm^2.

PACS number(s): 12.15.Ff, 14.60.Gh

I. INTRODUCTION

In the present day standard model of fundamental interactions, neutrinos are presumed to be massless. Furthermore, the neutrino species associated with each lepton generation is unique. There is no mixing of the species, unlike the quark sector where "flavor" mixing is characterized by the familiar Kobayashi-Maskawa (KM) matrix. It is essential that these assumptions regarding neutrino properties be experimentally examined, as any

small discrepancy could be an important clue to the structure of the fundamental interactions [1].

Nonzero neutrino masses have not been established through direct mass-measurement experiments. The present limits for the ν_e, ν_μ, and ν_τ masses are 9.3 eV/c^2 (95% CL), 270 KeV/c^2 (90% CL), and 35 MeV/c^2 (90% CL), respectively [2]. Similarly, lepton flavor mixing has not been observed in the decays of the charged leptons. For example, the experimental upper limit on the branching ratio of the decay $\mu \rightarrow e\gamma$ is 4.9×10^{-11} (90% CL) [3].

Important tests of these two issues can be made by searching for evidence of neutrino oscillations [4]. If neutrinos have finite masses and the neutrino states that couple in the weak interaction are not identical to the mass eigenstates, then "oscillations" between neutrino species will be a natural consequence. In the simple model, with only two neutrino flavors, ν_α and ν_β, and with mass eigenstates ν_1 and ν_2, we have

$$|\nu_\alpha\rangle = \cos\theta|\nu_1\rangle + \sin\theta|\nu_2\rangle \ ,$$

$$|\nu_\beta\rangle = -\sin\theta|\nu_1\rangle + \cos\theta|\nu_2\rangle \ ,$$

where the mixing angle θ is analogous to the Cabibbo angle. If the masses m_1 and m_2 are small compared to the total energy E, then the probability that neutrino species ν_α behaves instead like ν_β after traveling a distance L is

---

*Present address: Physics Department and Lawrence Berkeley Laboratory, University of California, Berkeley, CA 94720.

†Present address: Rensselaer Polytechnic Institute, Troy, NY 12180-3590.

‡Present address: University of Alberta, Edmonton, Alberta, Canada T6G 2J1.

§Present address: Southern University, Baton Rouge, LA 70813.

**Present address: EG&G, Los Alamos, NM 87544.

††Present address: McGill University, Montreal, Quebec, Canada H3A2T8.

‡‡Present address: CEBAF, Newport News, VA 23606.

§§Present address: Tufts University, Medford, MA 02155.

$$P(\nu_\alpha \rightarrow \nu_\beta) = \sin^2(2\theta)\sin^2(1.27\delta m^2 L/E) , \qquad (1)$$

where $\delta m^2 \equiv |m_2^2 - m_1^2|$ is in eV^2 and L/E is measured in m/MeV (or km/GeV). Experimental limits on the oscillation probability $P(\nu_\alpha \rightarrow \nu_\beta)$ restrict the unknown parameters $\sin^2(2\theta)$ and δm^2.

In approaches that are commonly called "appearance" or "exclusive" experiments, one prepares a particular neutrino species and searches for another. In a "disappearance" or "inclusive" experiment, one searches for evidence of a discrepancy with the expected flux of a specific species attributable to neutrino oscillations. Experiments have been performed with several different neutrino sources but there is no established evidence for neutrino oscillations [5]. The best limits come from searches for $\bar{\nu}_e$ disappearance at nuclear reactors [6] and from searches at high-energy proton accelerators for ν_μ and $\bar{\nu}_\mu$ disappearance [7] and ν_e, $\bar{\nu}_e$, and ν_τ appearance [5,8–12] Usually these experiments are analyzed in terms of oscillations between flavor eigenstates, but oscillations of the type $\nu \rightarrow \bar{\nu}$ between neutrinos with the same or different flavors are also possible [13]. An investigation of $\nu \rightarrow \bar{\nu}$ oscillations was conducted using high-energy accelerator-produced neutrino beams by Cooper *et al.* in 1982 [14]. In addition, the results of the pioneering experiment searching for ^{37}Ar production from $\bar{\nu}_e$ absorption on ^{37}Cl near a reactor [15] can be interpreted as a limit on $\nu_e \rightarrow \bar{\nu}_e$ oscillations [16].

We have searched for $\bar{\nu}_e$ appearance at the Los Alamos Meson Physics Facility (LAMPF) using a 20-ton neutrino detector consisting of liquid scintillation counters and proportional drift tubes. The results of the present experiment (LAMPF experiment E645) obtained after the first year of running were published previously [17]. In this paper we report on the data obtained during the entire three years of the experiment, 1987 through 1989.

The neutrinos radiated from the LAMPF proton beam stop come from the weak decays of nearly thermalized π^+ and μ^+ and, to a good approximation, the beam stop is a copious source of ν_e, ν_μ, and $\bar{\nu}_\mu$, but no $\bar{\nu}_e$. Our detector is primarily sensitive to $\bar{\nu}_e$, detected via inverse beta decay, $\bar{\nu}_e + p \rightarrow e^+ + n$, and thus we test for $\bar{\nu}_e$ appearance from any of the other three types of neutrinos. The primary experimental signal is the observation of the final-state positron. In this paper we describe a search for $\bar{\nu}_e$ appearance with two methods: in the first, we search for an excess of beam-on events with a positron whose energy is consistent with a transformed neutrino from the beam interacting by inverse beta decay; and in the second, we also require evidence for the final-state neutron in inverse beta decay. The second method has a lower efficiency, but the neutron requirement removes significant backgrounds from elastic scattering of ν_e, ν_μ and $\bar{\nu}_\mu$ on electrons and ν_e scattering on complex nuclei. Cosmic-ray events in the detector are the most serious background. The cosmic-ray trigger rate alone could overwhelm the data acquisition electronics. Cosmic-ray-induced triggers are reduced to an acceptable level with the aid of an active cosmic-ray shield. An "event history" of each trigger includes the signals produced in the detector and shield for a period before and after each

trigger. The event histories are essential for eliminating the background events which result from cosmic-ray muons which stop and subsequently decay in the detector. Positron tracks in the detector are distinguished from background proton tracks, induced mostly by cosmic-ray neutrons, on the basis of measurements of the differential and the total energy loss. It should be noted that our detector cannot distinguish between electrons and positrons.

II. THE EXPERIMENT

Figure 1 shows the position of the E645 apparatus relative to the LAMPF beam stop. The mean distance of the central detector from the neutrino source is 26.6 m. The experiment is located in a tunnel under an iron and earth overburden of approximately 2000 g/cm^2.

In the following subsections we describe the LAMPF beam-stop neutrino source and our experimental apparatus. A detailed description of the operation and the calibration of the beam-stop neutrino source is found in Refs. [18,19]. A more complete description of the E645 experimental setup is included in Refs. [17,20–22].

A. The LAMPF A-6 neutrino source

The LAMPF proton linac delivers a 797-MeV beam with average peak currents that can exceed a milliampere. The linac duty cycle is rather long and thus it is not well suited to neutrino experiments. The ~ 800 μs long beam bunches are spaced at 120 Hz. Typically $\frac{1}{3}$ of the beam pulses are diverted to other experimental areas. An additional 20% of the beam intensity and 20–30 MeV of beam energy are lost in upstream pion production targets; the remaining beam is absorbed on the A-6 beam stop, shown schematically in Fig. 2.

The protons produce secondary pions in the beam stop; the π^0 decay almost immediately to gamma rays, nearly all of the π^- are captured by nuclei, but most of the π^+ lose energy by ionization before decaying. The dominant
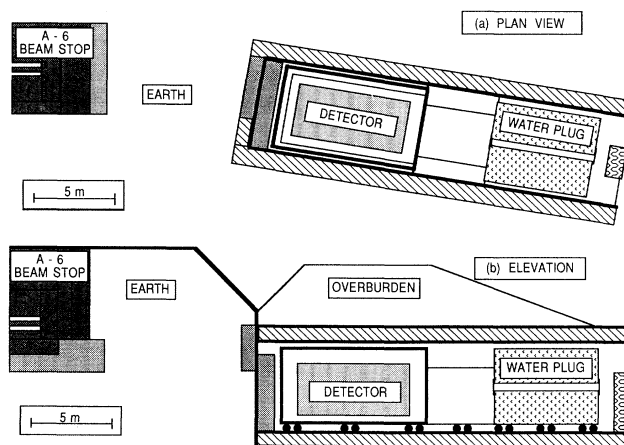

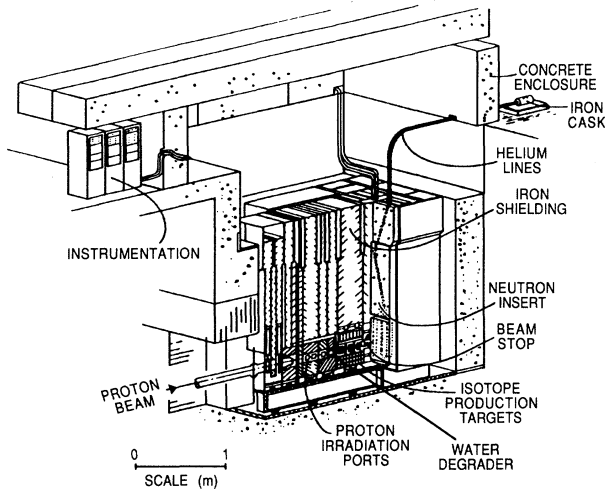FIG. 1. Plan and elevation views of the detector and shielding.

FIG. 2. Typical configuration of the LAMPF beam stop. Most of the pion production occurs in the water degrader and isotope production stringers.

decay mode, $\pi^+ \to \mu^+ \nu_\mu$, is followed by $\mu^+ \to e^+ \bar{\nu}_\mu \nu_e$, resulting in equal numbers of ν_μ, $\bar{\nu}_\mu$, and ν_e. Figure 3 shows the neutrino energy spectrum from π^+ and μ^+ which decay at rest. Because the π^- are absorbed, the $\bar{\nu}_e$ flux from the beam stop is less than 5×10^{-4} of the ν_e flux [18]. High-energy neutrinos which comprise about 2% of the total neutrino flux, arise from the small fractions of the pions that "decay in flight." These decay-in-flight neutrinos have a wide range of energies; they are a useful source of high-energy-neutrinos, but they are a potential source of background for the present measurement.

The critical factor determining the ultimate neutrino flux from the beam stop is the ratio of π^+ decays per incident proton. This ratio depends on the composition and geometry of the beam stop. The important com-
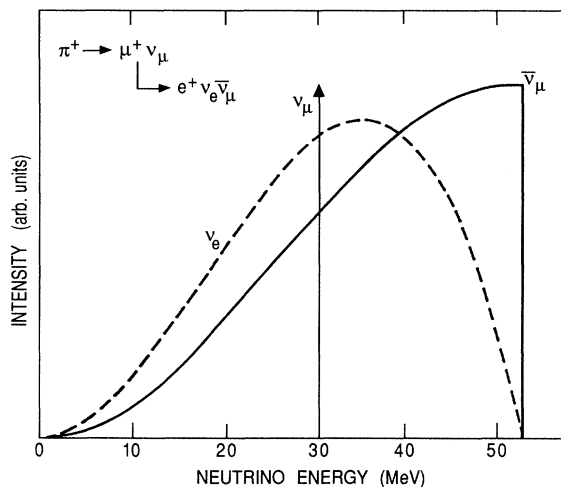
ponents of the A-6 beam stop [23] that are struck by the proton beam include the vacuum windows, a water beam degrader, material associated with isotope production, and a water-cooled copper "beam dump" which absorbs most of the beam power. The 20-cm-long water degrader is a region with high pion production, but low pion absorption, important for optimizing the neutrino yield. The beam stop is also a facility for producing radioisotopes. Various materials contained in mechanisms called "stringers" are periodically inserted into the beam. The number of inserted stringers and the particular materials being irradiated varied during the experiment. The beam dump consists of copper plates enclosed in a water-cooled stainless-steel jacket.

The neutrino flux for each of the approximately eight-week-long LAMPF running cycles was computed with the aid of a Monte Carlo simulation program which accurately accounted for the geometry and composition of the beam stop, including the changing stringer configuration [19,24]. The program calculated the propagation of protons and pions through the various materials, accounting for the possible interactions and decays. The energy and media dependencies of these processes were taken from measurements of proton-induced pion production and pion decay in thick targets. The Monte Carlo procedure was tested and calibrated in a separate experiment which measured pion production in a mockup of the beam stop [18]. The absolute normalization of the resultant neutrino flux was determined from that experiment (LAMPF experiment E866).

The calculated spatial distributions of pion decays in the beam stop for cycles 48 and 55 are shown in Fig. 4. The effect of the water degrader, at the 90-cm position, in

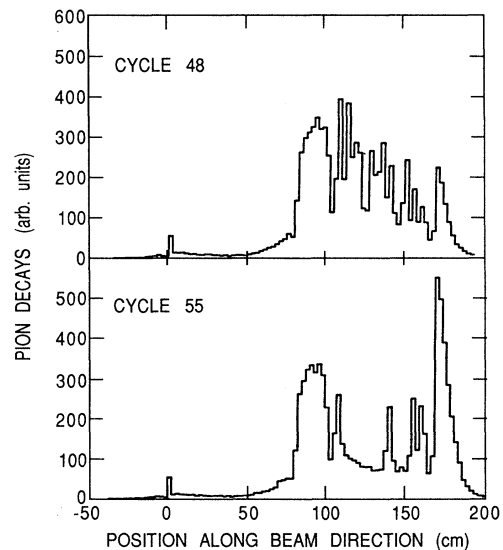FIG. 3. The neutrino energy spectrum from the decays of stopped π^+ and μ^+.

FIG. 4. The distribution of pion decays along the beam direction for cycles 48 and 55, which have different beam-stop configurations. The front of the water degrader is at 80 cm. The proton beam energy is 772 MeV for both cycles. During cycle 55, stringers 2, 3, 4, 5, and 7 were extracted from the beam.

TABLE I. The composition of the LAMPF beam stop for running cycles 48 through 55, corresponding to the beam delivered during 1987, 1988, and 1989. The water degrader target is absent for two periods, 50b and 51b, resulting in a 30% decrease in the neutrino flux. Variations in the composition of the isotope production stringers changed the neutrino flux normalization by a few percent. See Fig. 2 for the location of the ports and stringers.

Cycle	Proton energy (MeV)	Number of filled proton irradiation ports	Number of stringers	Water degrader	π^+/p	Integrated current (Coulombs)
48	772	0	9	IN	0.087	1326
49	783	1	9	IN	0.091	1871
50a	772	1	8	IN	0.090	1437
50b	772	1	1	OUT	0.060	492
51a	783	0	9	IN	0.092	1249
51b	783	0	9	OUT	0.071	585
52	783	0	4	IN	0.088	2541
53	767	0	5	IN	0.084	769
54	772	2	5	IN	0.086	1639
55	772	1	4	IN	0.084	1871

enhancing neutrino production is evident in the figure. During the course of the experiment, the flux at the detector was typically 6×10^6 sec^{-1}cm^{-2} for each neutrino type.

The necessary input data for determining the neutrino flux is given in Table I. Separate entries are given for periods when the water degrader is inserted and when it is removed since it had a substantial effect on neutrino production. It is also necessary to account for the thickness of the upstream production targets since this affects the energy of the incident protons. The integrated proton flux for the entire experiment is 13 871 Coulombs. The average of the calculated number of π^+ decays per proton, weighted over the course of the experiment is 0.086. The resulting determination of the integrated neutrino flux is assigned an 8% uncertainty; the error is dominated by the systematic uncertainties in the experiment which calibrated the beam stop [18].

B. The detector

We are sensitive to $\bar{\nu}_e$ in the beam through the inverse beta decay reaction on protons in the detector,

$$\bar{\nu}_e + p \rightarrow e^+ + n \ . \tag{2}$$

As previously noted, our detector does not distinguish e^+ from e^- and in the following we will refer to them collectively as "electrons." The central detector consists of 40 planes of liquid scintillator counters and 41 vertical and 41 horizontal planes of proportional drift tubes (PDTs).

The inner detector is described in detail in Ref. [20]. The liquid scintillator, predominantly CH_2 in the form of mineral oil, provides most of the target protons for neutrinos. The detector is configured in repetitive units, each consisting of a scintillator plane and one "x" and one "y" PDT plane. Figure 5 shows an expanded view of a PDT-scintillator subunit. A liquid scintillator plane consists of twelve cells, with the scintillator contained in

extruded acrylic tanks with 0.32-cm-thick walls. The individual counters are 30.5 cm high, 366 cm long, and 3.63 cm thick in the direction of the incident neutrino beam. A 5-cm-diam Hamamatsu R878 photomultiplier tube (PMT) views the scintillator from each end.

A PDT plane has 45 cells, each one 7.62 cm high, 366 cm long, and 3.81 cm thick. The PDTs are constructed from rectangular tubes of 0.17-cm-thick laminated cardboard impregnated with epoxy. The inner surfaces are covered with 33-μm-thick aluminized mylar serving as a vapor barrier for the contained P-10 gas mixture (90% argon and 10% methane) and as a ground plane for the PDT electric field. The use of cardboard instead of a metal such as aluminum is part of the effort to reduce backgrounds by avoiding materials with large ν_e cross
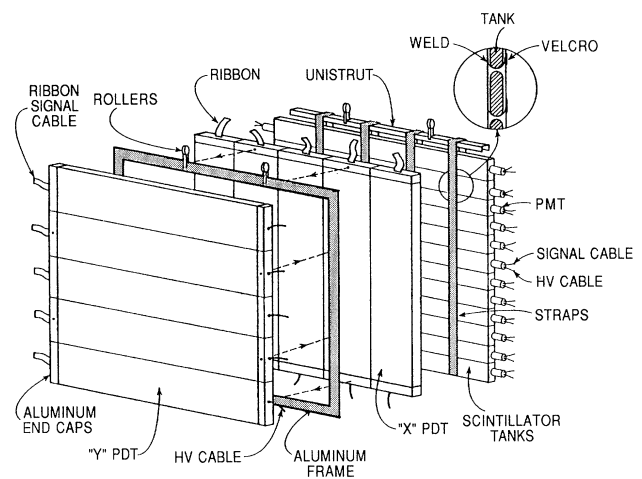

FIG. 5. Expanded view of one plane of the detector showing Proportional Drift Tubes (PDTs) and a liquid scintillator hodoscope. There are a total of 40 such units.

TABLE II. Number of atoms and electrons in the detector within the 366 cm × 366 cm area of the 40 scintillator planes and 41 paris of PDT planes.

Material	e (10^{30})	H (10^{30})	C (10^{29})	O (10^{29})	Al (10^{27})	Gd (10^{26})
Scintillator	4.45	1.12	5.55			
Lucite	1.46	0.22	1.36	0.54		
Mylar	0.17	0.01	0.17	0.07		
Cellulose	1.35	0.16	0.94	0.78		
Aluminum	0.08				6.35	
Gadolinium oxide	0.02			0.00		2.05
TOTAL	7.44	1.51	8.02	1.40	6.35	2.05

sections. A single 50-μm-diam gold-plated tungsten sense wire is stretched the length of each PDT.

The 0.127-mm-thick mylar sheets, coated with a 5.8-mg/cm^2-thick layer of gadolinium oxide (Gd_2O_3), are inserted between the scintillator and PDT planes to facilitate neutron detection from inverse beta decay. As described below, the gamma rays from thermalized neutrons which capture on Gd are identified as a delayed signal in the liquid scintillator counters.

The material composition of the detector is summarized in Table II. Whenever possible detector materials were carefully selected to reduce backgrounds from neutrino nucleus scattering. Moreover, electrons in the energy range of interest (less than 60 MeV) do not often create electromagnetic showers because the detector is composed mostly of low-Z materials. The signature for a low-energy electron produced by a neutrino is a nearly straight track with minimum ionization energy loss along its length. The typical electron path length is $\sim$4 planes. A normally incident electron would span $\sim$7–8 planes. The average of the energy loss in the scintillators gives the differential energy loss. The sum gives the total energy. The differential energy-loss measurement allows us to distinguish protons from electrons. We expect to misidentify a proton as an electron only about 1 time in 10^3 using just data from the scintillators. Energy-loss information obtained from the PDTs improves are ability to distinguish between electrons and protons.

For each event trigger we record the pulse heights of all scintillation and PDT detectors from 56.7 μs before to 110 μs after the trigger. We use the first period to search for evidence of stopped-muon backgrounds. The data in the second period contains the signals from neutron capture on Gd.

Figure 6, taken from our on-line event display, shows the characteristic pattern of a stopped muon which eventually beta decays inside the detector. In this event, the track from the beta-decay electron is delayed by 3.2 μs from the signals of the stopping muon.

The signals from the PMTs and PDTs are shaped with 300 ns rise times and 1.5 μs fall times, then digitized by flash analog-to-digital converters (FADC) and stored in individual random access memories (RAM) which operate as circular buffers. Two RCA-3300D 6-bit FADCs with overlapping ranges cover the energies expected in this experiment. The low- and high-level

FADCs have individual ranges corresponding to 0–2 times and 2–15 times the energy deposition of a minimum ionizing particle. The time between digitizations is 81.3 ns. Digitization is halted 110 μs after a valid trigger is detected. The time of the triggering event is known with an accuracy of about 100 ns. All the finite digitizations within 1 μs of the trigger time are assumed to be a feature of the primary triggering event.

Neutrons produced from the process $\bar{\nu}_\mu \to \bar{\nu}_e$ followed by $\bar{\nu}_e + p \to e^+ + n$ have energies up to 5.2 MeV. These energetic neutrons are moderated in the detector and a significant fraction are captured by the Gd nuclei within the 110 μs post trigger window. On the average, the capture reaction leads to 8 MeV divided among slightly more than four gamma rays. The neutron detection efficiency is monitored periodically with the aid of a ^{252}Cf source. Fragments from spontaneous fission register in an ion chamber which generates a trigger for the detector. The capture time distribution is shown in Fig. 7. The neutron detection efficiency is $\sim$30%.

The usual experimental trigger condition is defined by coincident hits in three out of any four contiguous scintillation planes. A scintillation "hit" is a signal in both
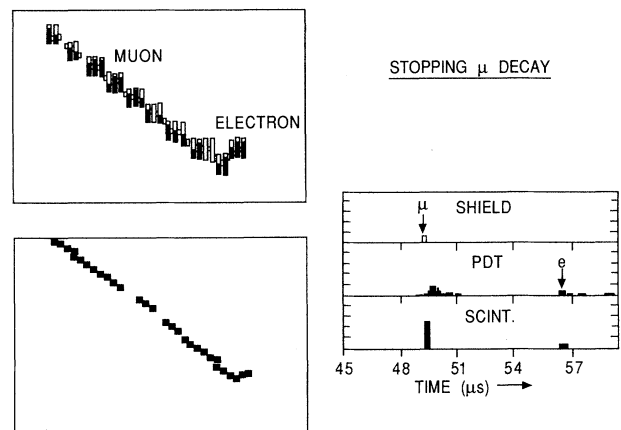

FIG. 6. On-line display of a $\mu \to e$ decay showing the side and top view and the time distribution of the signals. Large rectangles represent scintillation counter signals and small rectangles PDT signals.
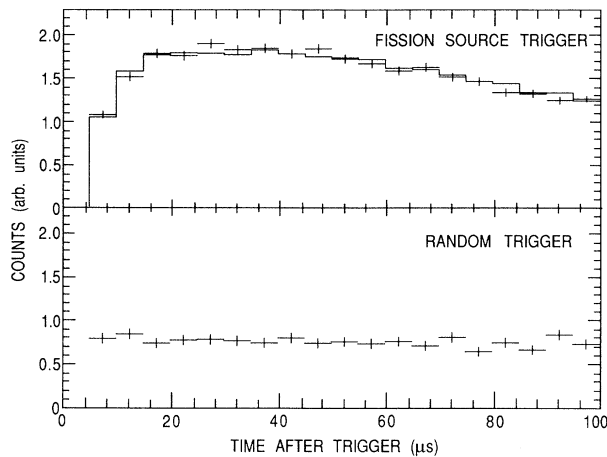
FIG. 7. Detector time history for a tagged neutron source trigger and for a random trigger. The solid line is a Monte Carlo calculation.

PMTs at least a fifth as large as that of a minimum ionizing particle which traverses the middle of the cell. A trigger is electronically vetoed if there is a hit in the active shield during the previous 11 μs. A shorter, 2.5-μs veto is imposed if there are hits in multiple sections of the shield, on the assumption that a muon passed through without stopping. The average data acquisition dead time is about 16% at the typical instantaneous trigger rate of 0.6 Hz. Data taking is active during the 0.8-ms beam pulse (called the "beam-on" gate), and for a preceding 1.0-ms period ("prebeam" gate) and a subsequent 1.0-ms period ("postbeam" gate), allowing cosmic-ray background subtraction. A variety of additional "special triggers" are also provided. The special triggers include a random trigger to study the accidental background, and the trigger from the ^{252}Cf calibration source described above.

Calibration data samples are obtained periodically using one of the special triggers. Samples of cosmic-ray muons are used to study the response of each element of the detector [20]. The scintillation light yield for normally incident cosmic-ray muons is determined using the tracking feature of the detector. The pulse height distribution for these muons which passed through the center of one scintillation counter is shown in Fig. 8. The peak of the distribution corresponds to a detected energy loss of 4.9 MeV. When the detector is operated with only a 2.5-μs-long shield veto, the triggers are nearly all from stopped-muon decay electrons. Figure 9 shows the histogram of the time difference between the trigger and earlier hits in the event history after the short veto. The time difference is characteristic of a muon which enters the detector, but is prevented from triggering the detector by the short veto. The muon eventually stops and the beta-decay electron generates the trigger. Fitting the distribution with the function $Ae^{-t/\tau}+B$ gives $\tau = 2.10\pm0.02$ μs, consistent with the average $\mu^{\pm}$ lifetime expected in the material comprising the detector [20].

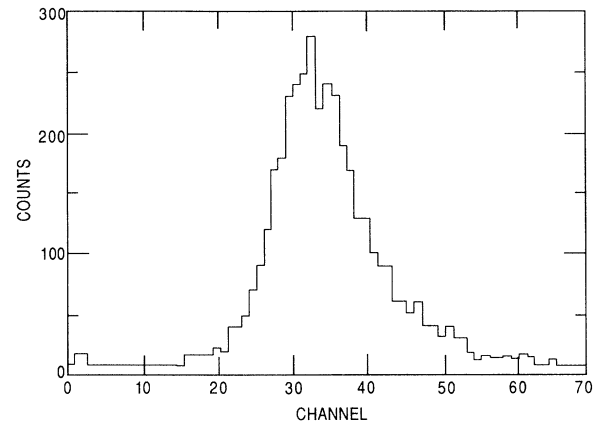The response of the detector to neutrino interactions and muon decay are modeled with a Monte Carlo tech

nique. Electrons and photons are described with the well-known EGS4 code [25]. Neutron propagation through the various detector components is modeled according to a program which incorporates measured neutron-elastic-scattering and neutron-capture cross sections [26]. The neutron detection efficiency measured with the ^{252}Cf source is reproduced by the simulation and the calculated thermalization time of 16 μs is consistent with our observations. The detector efficiency and the analysis efficiency are studied with the aid of Monte Carlo generated events. These events are combined with randomly triggered events before analysis. This procedure gives the correct analysis efficiency and correctly accounts for the effect of the backgrounds.

The input data for the Monte Carlo simulation is updated for each running period to represent the actual state of the detector. The typical PDT efficiency is 94%,

FIG. 8. Pulse height distribution in a scintillator module for normally incident through-going muons.
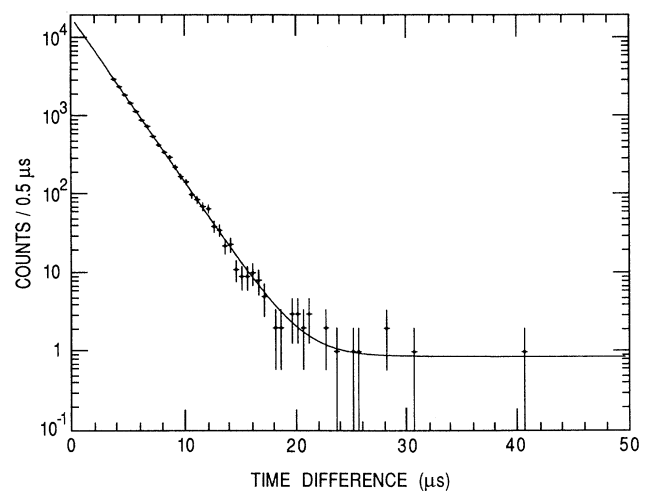

FIG. 9. Time difference distribution for muons stopping in the central detector. The solid line is the result of a fit to an exponential plus a constant background function. The fitted lifetime of 2.10 ± 0.02 μs agrees with that expected for $\mu^{\pm}$, including μ^{-} capture in the detector.
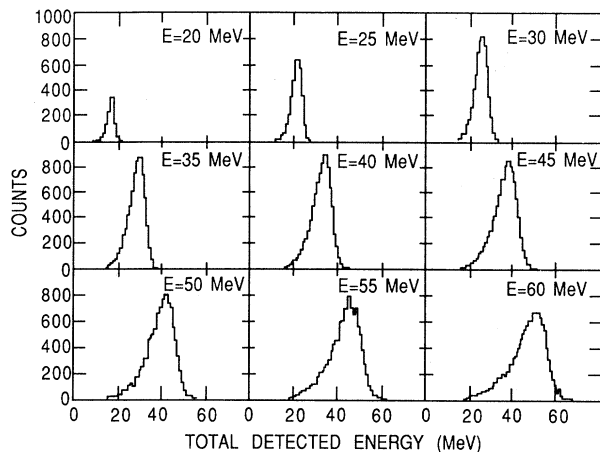
FIG. 10. Detector response to electrons calculated with a Monte Carlo simulation assuming an isotropic distribution.

including the losses from inoperative channels. At any given time about 5% of the scintillation counters were inoperative. Figure 10 shows the simulated detector response to electrons with energies between 20 and 60 MeV. The total electron energy for real events is based on the detected energy after correcting for the effects of passive materials along the track.

Samples of stopped-muon beta-decay electrons provide the best check of the detectors' response to electrons. The Michel energy spectrum of electrons from muon beta-decay closely resembles the distribution expected from $\bar{\nu}_\mu$ oscillations into $\bar{\nu}_e$ followed by inverse beta decay. Figure 11 demonstrates good agreement between energy distributions of stopped-muon beta decay and the
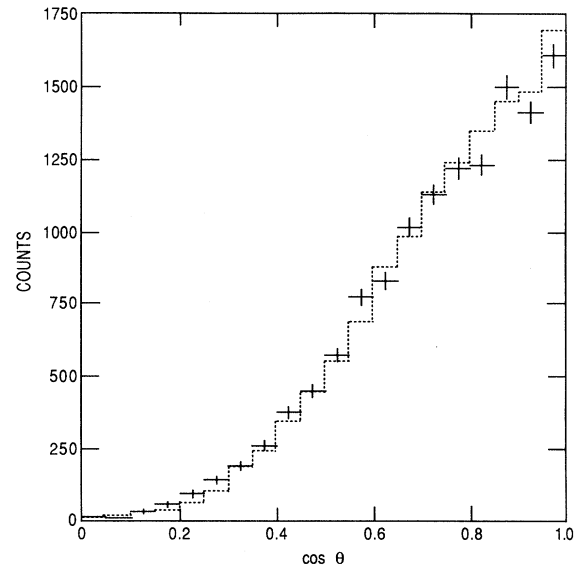
FIG. 12. The distribution in $\cos\theta$ of electrons from muon decays compared with a Monte Carlo simulation (dashed histogram). The angle θ is measured with respect to an axis pointing from the beam stop to the track endpoint nearest the beam stop.

Monte Carlo simulation over most of the energy range. Figure 12 indicates that the angular acceptance of the detector is also well characterized.

The stopped-muon decay data sample is also useful for checking the efficiency of the trigger electronics. The scintillation-counter trigger discriminator status is recorded for each event. This information is compared to the corresponding pulse heights and the efficiency of each detector in the trigger is accurately characterized. A slight variation in the longitudinal distribution of the locations of the triggering track observed in the stopped-muon decay data is quite consistent with the predictions of the Monte Carlo simulation. The observed spatial variations are attributable to inefficient or inoperative detector modules.

C. Cosmic-ray shielding

The design of the experiment is strongly influenced by the need to suppress the cosmic-ray backgrounds. The LAMPF's large duty factor is long, about 6%, and we would expect about 1.6×10^7 events from cosmic-ray muons each day. About 2% of the muons stop and decay in the detector. It is essential that these decays be identified because, as previously noted, the muon-decay electrons simulate the neutrino oscillation signal. The active cosmic-ray shield, described below, serves both to reduce the muon trigger rate and aids in suppressing the background from stopped-muon beta decay.

The active veto shield is a semicontinuous cylindrical volume of liquid scintillator (Bicron 517P), 15 cm thick, viewed by 360 12.5-cm-diam EMI-9870B hemispherical PMTs. The inside surfaces of the scintillator container are coated with a highly reflective white paint that is compatible with the chemically aggressive liquid scintilla-
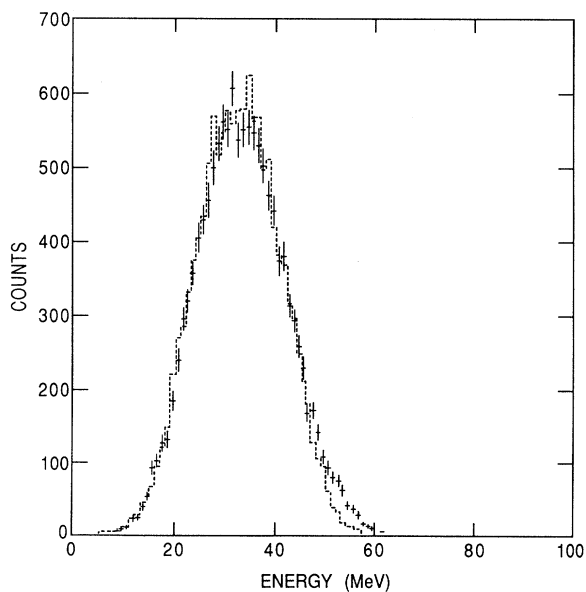
FIG. 11. Total energy along electron tracks from stopped-muon decays. The energy is corrected for inactive material. The dashed line shows a Monte Carlo simulation.

tor. The outside of the tank measures 10.1 m long by 6.75 m diameter. Backing the scintillator tank is a concentric passive shield consisting of a 17.5-cm-thick volume filled with fine lead shot (packing fraction ≈ 0.7), constrained within two steel shells, each 1.7 cm thick. The passive shield absorbs gamma rays which might traverse the active veto shield without being detected. One of the backgrounds reduced by the lead is bremsstrahlung photons coming from decay electrons originating from those muons which stop and decay near the inner surface of the tunnel housing the experiment. The shield assembly is constructed in two major sections which ride on independent systems of rails. One section carries the bottom "cart" which supports the neutrino detector, a vertical circular wall, and the principal part of the electronics which is housed in a "hut" as shown in Fig. 13. For structural reasons the bottom cart is divided into 6 optically isolated sections, separated by I beams. The vertical wall is also optically isolated from the cart. The other major section supports the main part of the cylinder and the remaining vertical wall. This section forms a single, continuous liquid scintillator tank.

The active shield is a detector for charged cosmic rays, primarily muons. As noted it is essential to veto the muon triggers, but the event rate due to delayed triggers from stopped-muon beta-decay electrons would also be unacceptable. To minimize deadtime, this is achieved with two veto gates. A "long" veto (about 11 μs) is applied if a hit, presumably from a stopping muon, is detected in one and only one of the optically isolated sections of the shield. A "short" veto (about 2.5 μs) is applied for coincident hits in isolated sections on the assumption that the muon excited the detector. The general "hit" condition is specified by an adjustable number of hit PMTs (typically from 3 to 5) with signals above threshold.

The performance of the cosmic-ray shielding is discussed at length in Refs. [21,22] and we summarize the basic issues here. The online inefficiency of the active shield for detecting cosmic-ray muons is roughly 10^{-4}. Most of the inefficiency is from muons that hit the shield

but fail to pass the multiplicity condition which is always set to be greater than one. The missed muons generally hit the shield at the location of a PMT. For these hits the distance to the neighboring PMTs is maximized. Furthermore the PMTs protrude into the scintillator, reducing the scintillator thickness. Nevertheless, these events are easy to identify offline because a single PMT has an exceptionally large output pulse.

Most of the required reduction in the cosmic-ray rate is achieved in the offline data analysis. The active shield PMT signals are digitized and stored in RAM similar to the other detector signals. However, the shield signals are shaped with a 30-ns rise time and a 1.4-μs fall time; the digitizing period is 167 ns. A 56.7 μs of event history proceeding the time of the trigger is used as the basis of more stringent offline cuts as discussed below.

After stopping muons the next most serious cosmic ray background is from neutron generated events due to protons from *n-p* scattering. Recoil protons are heavily ionizing and easily discriminated from electrons, but the trigger rate must be acceptably low. More troublesome are the secondary reactions that can produce electron tracks and false neutrino signatures. Among these are gamma-ray producing nuclear reactions, the reaction $n + p \rightarrow np\pi^0$ where the π^0 photons scatter, and the $n + p \rightarrow nn\pi^+$ reaction, with an electron coming from the π to $\mu \rightarrow e$ decay chain. The only practical way to reduce the backgrounds from neutrons is with massive passive shielding.

The tunnel is covered by iron and earth at least 2000 g/cm^2 thick and a 720 g/cm^2 thick water tank seals the downstream end of the tunnel. The cosmic ray neutron flux is reduced by a factor of 2000. Figure 14 shows the decrease in the detection rate of recoil protons (our most sensitive measure of the neutron background) as passive shielding is added over the sides and downstream end of the detector during 1986 and 1987. The trigger rate from cosmic-ray neutrons is between 20 and 40 per live-time-equivalent day (≈ 5600 sec considering the LAMPF accelerator duty factor) for most running, depending somewhat on the energy range and the fiducial volume cut.
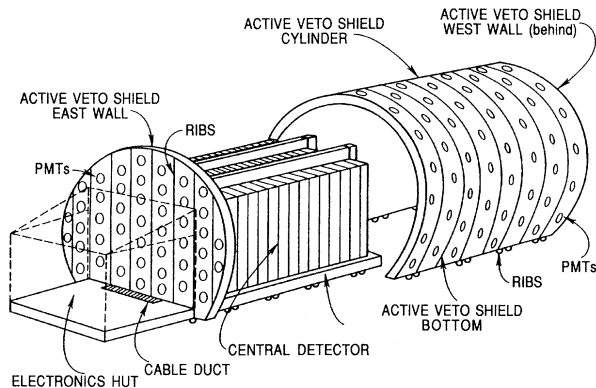

FIG. 13. Isometric view of the detector and cosmic ray shield. The bottom of the shield and one vertical wall move as a unit along with the central detector.
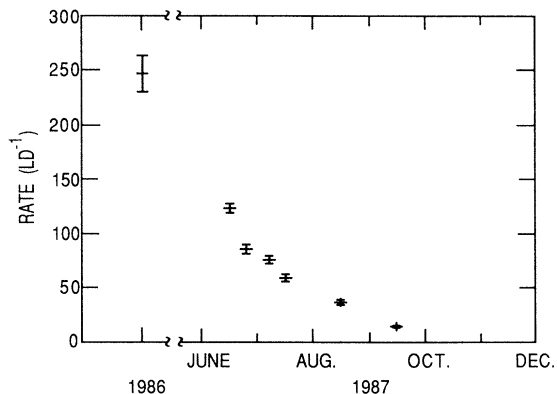

FIG. 14. Cosmic-ray *n-p* scattering rate during the period shielding is stacked over the detector. One LD (LAMPF day) corresponds to 5600 sec of beam time.

Interpreting the direction of the detected proton tracks to be the same as the incident direction of the neutron which scattered indicates that most of the neutrons come from the rear of the tunnel, where the shielding is weakest.

D. Beam shielding

It is essential that the detector be well shielded from the beam stop. In particular, there must be sufficient shielding to drastically reduce the flux of beam produced neutrons. There is approximately 15 m of tuff (volcanic debris) followed by 2 m of steel between the beam dump and the detector, providing an attenuation larger than 10^{17}. Nevertheless, when the experiment began in 1986 the beam-associated neutron background was unacceptably high. The high neutron background was subsequently attributed to a few weak spots in the shielding; when corrected the neutron rate was a factor of 1000 lower and at the expected level.

Figure 15(a) displays the distribution of detected energy for the recoil protons arising from elastically scattered cosmic ray neutrons. Figure 15(b) shows the difference between beam-on and beam-off runs for equal live time. The beam excess is insignificant and the neutron associated cosmic-ray rate is only about 7×10^{-3} sec^{-1}. The measured beam-associated excess of proton tracks is -0.9 ± 7.8 per kC of LAMPF beam. Thus there are less than 150 beam-associated events identified by detecting proton recoils in the entire data set, corresponding to 13.8 kC of beam. With electron-proton discrimination better than 10^{-3}, the neutrons produce a negligible background in the neutrino-induced event sample. From the observed recoil proton energy distribution we estimate that at most only one pion was produced by beam generated neutrons during the experiment.
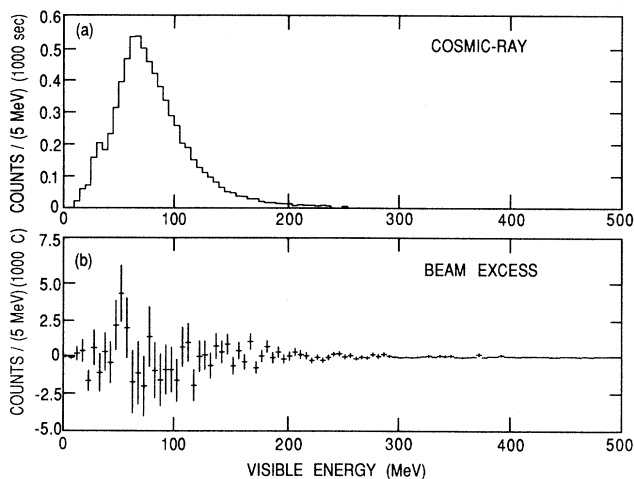

FIG. 15. Visible energy distribution attributed to protons from n-p scattering in the fiducial volume for (a) events in the cosmic ray gate and (b) beam excess events. The integral number of events in the beam excess is -0.9 ± 7.8 events/1000 Coulombs.

III. DATA REDUCTION

The raw data set consists of 2.5×10^6 events; most (78.8%) came during the beam-off gates. The total accumulated proton beam on the beam stop is 13 781 Coulombs for the beam-on live time of 1.19×10^6 sec. The total beam-off live time (the sum of prebeam and postbeam gates) is 4.44×10^6 sec.

In spite of the online veto and passive cosmic-ray shielding, most of the triggers are still caused by cosmic-ray events. These events can be categorized by their origin: cosmic-ray muons, electrons from stopped-muon decay, proton recoils from n-p scattering, and low-energy background events in which no track is visible in the detector. These background events are removed from the data set with softwave cuts based on the expected topology and characteristics of real neutrino events. We search for $\bar{\nu}_e$ appearance in two samples of beam-associated electron events, both with and without the signal of the residual neutron from inverse beta decay. We will describe the analysis without the neutron signal requirement first. To ensure the reliability of the conclusions, two completely independent analyses are carried out on the entire data set. The two analyses agree, increasing our confidence in the final conclusions. In this section we describe only one of the two procedures in which the constraints from neutron detection are not applied.

A. Shield veto at event time

The first cut is designed to eliminate events due to charged particles entering the detector from the outside. Occasionally, cosmic-ray muons trigger the detector but fail to be vetoed by the shield because two few active shield PMTs are hit. In the offline analysis the condition is strengthened and any event which has a "cluster" (i.e., group of *adjacent* PMTs) of two or more that were hit within one microsecond of the trigger is rejected.

B. Tracking and fiducial volume

Tracks are recognized on the basis of data from the PDTs and the scintillators. The software algorithm determines charged particle tracks by testing all possible end points and checking if the intermediate hits are collinear. At least two horizontal, and two vertical PDTs are required to establish a valid track. Frequently there are additional PDT hits away from the principal track due to delta rays. In these cases, the software algorithm chooses the combination of PDT hits which yields the most consistent track with all the data. Because multiple scattering dominates the angular resolution, the better spatial resolution obtained from the PDT drift time is not used at this stage in the analysis. As shown below, the tracking efficiency for real electrons is nearly 100%, yet a valid triggering track is found for only 60% of the triggers. This indicates that many of the triggers are not initiated by a single charged particle.

To assure that the event is fully contained within the detector volume, a fiducial volume cut is made on the track endpoints. Figure 16 shows the event distribution of the 1987 data after the obvious stopped-muon events
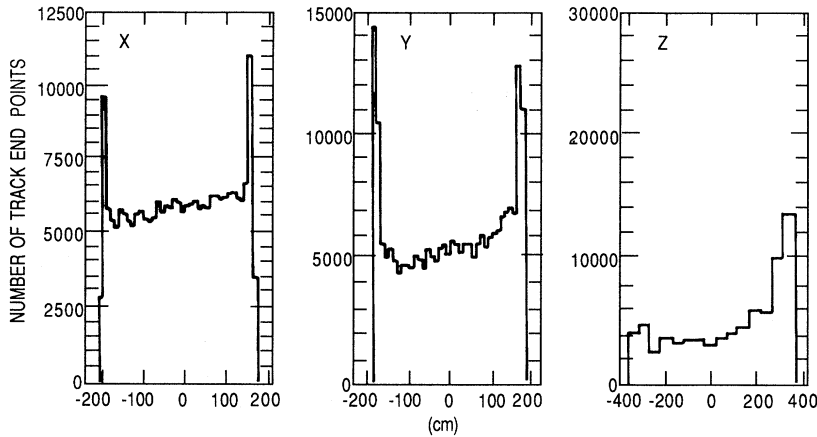
FIG. 16. Distributions of track endpoints for the 1987 data after the obvious stopped-muon events are removed.

are removed. Guided by these distributions the fiducial volume cut is taken to be 15 cm from the side edges, 20 cm from the upstream face, and 30 cm from the downstream face of the detector.

For each of the neutrino processes considered, the Monte Carlo simulation provides an estimate of the fraction of fully contained interactions which would trigger the hardware and be tracked by the software algorithms. These efficiencies are listed in Table III for the process $\bar{\nu}_e + p \rightarrow e^+ + n$. The tracking efficiency is 97±1% as measured with electrons coming from stopped-muon decays, in agreement with our Monte Carlo calculations. The systematic error in the trigger efficiency is estimated after considering the uncertainties in the scintillation counter responses and the observed spread of the trigger discriminator threshold settings.

C. Rejection of cosmic-ray muon decays

At this step in the analysis most of the events that remain are caused by cosmic-ray muons that stopped in the detector and the triggering track is the beta-decay electron. Most of the stopped-muon triggers come from muons that survive the 11-μs-long hardware veto before decaying. The veto time is extended to 30 μs in software, but to reduce deadtime additional requirements are applied to identify the initiating stopping muon.

A selected sample of very well characterized stopped-muon decays is obtained by searching the event history in

TABLE III. Trigger and analysis efficiencies for the reaction $\bar{\nu}_e + p \rightarrow e^+ + n$ for $\bar{\nu}_e$ coming from $\bar{\nu}_\mu$ to $\bar{\nu}_e$ oscillations.

Trigger efficiency	25.0±1.1%
Analysis efficiency	
Tracking	96.6±1.0%
Fiducial volume	69.3±0.9%
Stopped Muon/shield veto	73.4±1.2%
Particle Identification and associated energy	63.3±2.4%
Decay-in-Flight/past Hits	98.0±1.0%
Total analysis efficiency	30.5±1.4%

the 30 μs preceding the trigger for evidence of a well-defined muon track which is spatially correlated with the hits in the active shield and in the triggering track. This sample of selected events is very useful for calibrating the detector response to electrons. A search is also made for less obvious muon decays. Events are rejected if they contain earlier shield and detector hits which lie on a line which intersect a calculated end point of the triggering event's track. The shield hits are only required to have total pulse height above one-tenth of a minimum ionizing particle. Even with these procedures to remove cosmic rays, the number of background events is still unacceptable. Inactive detector materials and the small gaps between detector components allow a small fraction of the muons to stop in the detector without being detected. This background is suppressed to an acceptable level with cuts based on shield information alone. Events are eliminated if there is a previous localized hit in the shield with a pulse height sum corresponding to more than 12% of minimum ionizing. Figure 17 shows the time between the shield hit and the subsequent trigger. The discontinuities in the decay curve at 2.5 and 11 μs are artifacts of the hardware veto. After 11 μs the time distribution falls off with the same characteristic lifetime as in the sample of reliable stopped-muon events ($\approx 2.1\ \mu$s). The muon decay cuts and the strengthened prompt shield veto cut retain 73.4±1.2 % of valid the neutrino events. This efficiency is determined with a sample of randomly triggered events. The measured efficiency is checked by observing the number of lost events as the cuts are applied for periods longer than 30 μs. The error is predominantly statistical.

D. Particle identification and proton rejection

Events which satisfy the above criteria have well-contained tracks in the central detector and there is no evidence of previous activity in the detector or active shield. A large fraction of the electrons from neutrino interactions remain in the sample, but the background from recoil protons induced by neutron interactions have also been retained. The sample is also contaminated by photons which multiply Compton scatter in consecutive scin-
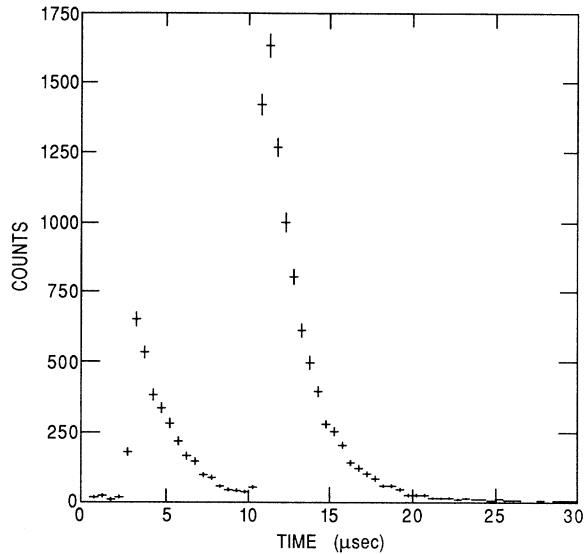
FIG. 17. Distribution of time differences between the trigger and the software veto. The suppression at times less than 2.5 μs is due to the online short veto, and at times less than 11 μs from the online long veto. The decay curves are consistent with stopping muon decay.

tillation counters, simulating a contained electron track. In this section we describe the procedures which find the true electron tracks.

Electron identification is based on differential energy loss in the scintillators and PDTs. We construct likelihood functions L_{SCI} and L_{PDT} based on the probability that the energy loss signals in the scintillators or PDTs is consistent with the known energy-loss distributions observed from the sample of reliable electrons from stopped-muon decay. This is shown in Fig. 18. Both the scintillator and PDT confidence level projections are uni-
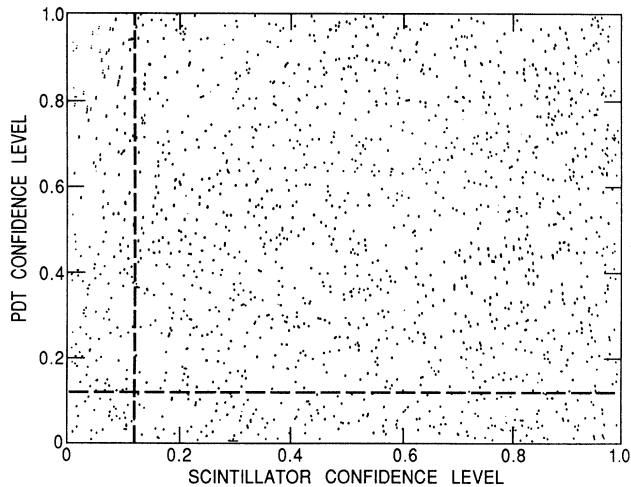
form and there is no evidence of any correlation between them.

This same confidence level analysis is applied to the reduced event sample. Most of the events show characteristic PDT- and electron-confidence levels below 0.05. This is in contrast with the distribution in Fig. 18 indicating that most of the events contain proton tracks. Figure 19 shows the scintillator and PDT electron-confidence levels for our 1987 event sample. To insure a clean electron signal, we demand that both confidence levels be greater than 0.12.

The scintillation counters at the end of the track are used in the likelihood calculation only if the outboard PDT is hit, indicating that the particle passed completely through the scintillation counter. If this condition is not satisfied, we require that the scintillator to have a signal smaller than 1.5 times that of a minimum ionizing particle. We also require that none of the scintillation counters and at most one of the PDTs on the track have a signal greater than four times that of a minimum ionizing particle. These last two conditions further reduce the number of proton tracks that remain in the sample.

The total energy of an event is taken as the sum of the energy deposited along the track and the "associated energy" that is deposited away from the track. Figure 20 shows the associated energy distributions for electrons in the stopped-muon decay sample and the final beam-on and beam-off samples. Studies of data taken in 1986 when the beam neutron background was large indicates that neutron interactions frequently have a large fraction of associated energy. We therefore require that the associated energy be less than 19.2 MeV, removing a few events from the sample. Finally, the total energy is required to be less than 60 MeV.

The fraction of real electron tracks that survive the particle identification and the energy selection criteria is checked using the stopping cosmic-ray muon sample. In all, 63.3±2.4% of these electrons survive the cuts. The

FIG. 18. Confidence level distribution for electrons from muon decay. The dashed lines indicate the cut for particle identification (CL > 0.12).
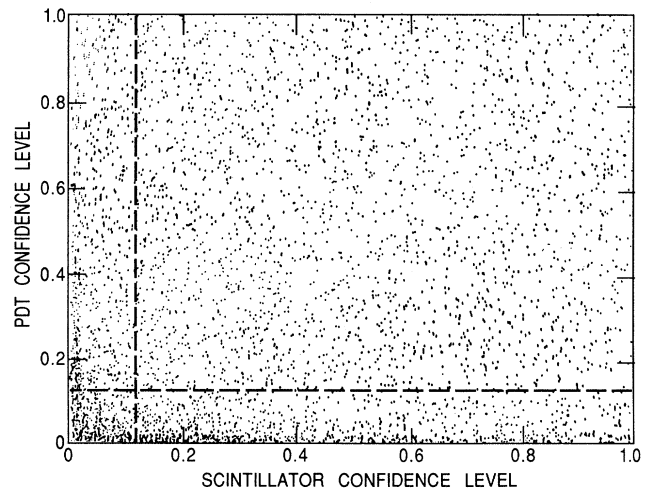

FIG. 19. Confidence level distribution for the beam excess data sample. The dashed lines indicate the cut for particle identification (CL > 0.12).
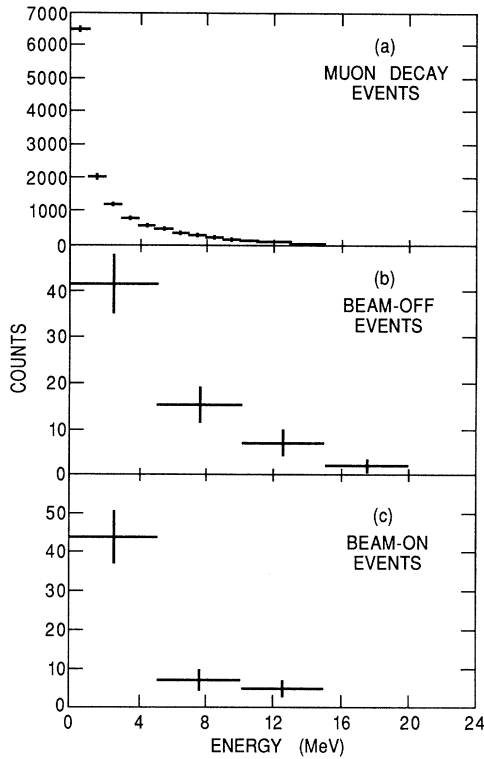
FIG. 20. Associated energy (energy deposited away from the observed track) for (a) electrons from muon decay, (b) beam-off events, and (c) beam-on events.
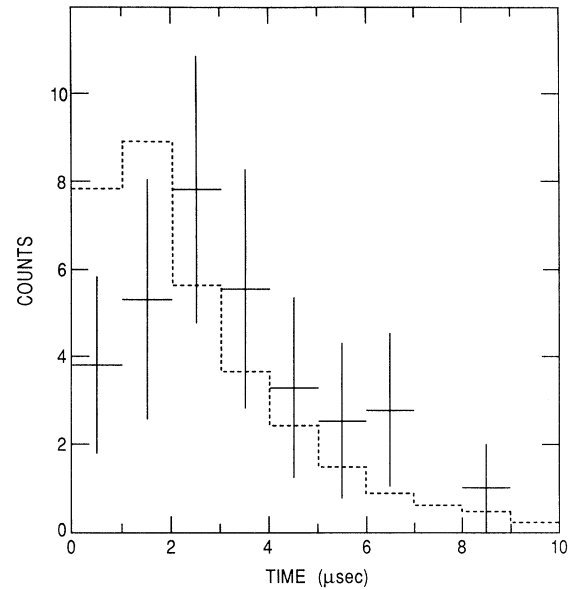

FIG. 21. Time distribution between triggering tracks and precursor detector hits. The observed distribution is evidence that these events arise from decay-in-flight neutrino produced muons. The histogram is a Monte Carlo simulation of this process.

systematic error estimate is based on the calibration uncertainties of the detector elements. At this stage an enhancement inside the beam-on gate begins to be evident. There are 110 beam-on events and 138 beam-off events; the beam-on live time is only 26.8% that of the beam off.

E. Decay-in-flight neutrino events

A small fraction of the $\pi^{\pm}$ produced at the beam-stop decay-in-flight, yielding energetic ν_{μ} and $\bar{\nu}_{\mu}$ which can produce $\mu^{\pm}$ in the central detector. Most have too low an energy to trigger the detector, but a $\mu^{\pm}$ can beta decay and be mistaken for a neutrino oscillation event. Most of these events are identified by searching the 20 μs of the event history preceding the trigger for muon signals in the scintillators and PDTs close to the triggering track. The following criteria were used to identify $\mu^{\pm}$ beta-decay events: that the preceding event history contain (a) a scintillator signal (greater than 0.8 MeV) or (b) at least 2 PDT hits (one PDT within 35 cm of an endpoint). If all hits are within the fiducial volume, the event is assumed to be from a decay-in-flight neutrino interaction, otherwise it is taken to be from stopping muon decay. In either case, the event is rejected. The time distribution of the muon precursors for the ~31 resulting beam-excess decay-in-flight candidates is shown in Fig. 21.

This cut for events with hits in the past rejects some of the events due to neutrinos from stopped pion decay.

From a study of a sample of background proton events, all of which should pass this cut, we conclude that about 2% of the ν_e and $\bar{\nu}_e$ initiated events are accidentally rejected.

Some decay-in-flight events are missed by the above procedure. Some muons, particularly those with very low kinetic energy, produce signals in the scintillators and PDTs too weak to be detected. Also, some muons decay too quickly to be time resolved from the triggering track. We resort to a Monte Carlo calculation to estimate the ratio of identified to unidentified decay-in-flight events in the final sample. From this ratio and the observed number of 31.3 ± 6.3 decay-in-flight events, we conclude that the final sample has 5.5 ± 2.3 undetected decay-in-flight events. This procedure uses the Monte Carlo simulation to estimate only the ratio and not the absolute number of decay-in-flight events. The previous event selection procedure should find most events triggered by a decay-in-flight produced muon, and, as expected, none of the events in the final sample show any indication of a delayed track from beta-decay. For those events where the muon is not time resolved from the electron, the Monte Carlo simulation indicates that 90% would be rejected by selection criteria on total energy, associated energy, or particle identification. The major uncertainty comes from not knowing the precise shape of the muons kinetic energy distribution which is estimated with a fermi gas model for ^{12}C (Ref. [27]). Allowing for the large uncertainty in the μ-energy distribution, we assign a conservative uncertainty of 2.3 events. Figure 22 shows good agreement between the observed and calculated muon-energy distribution for these decay-in-flight events.
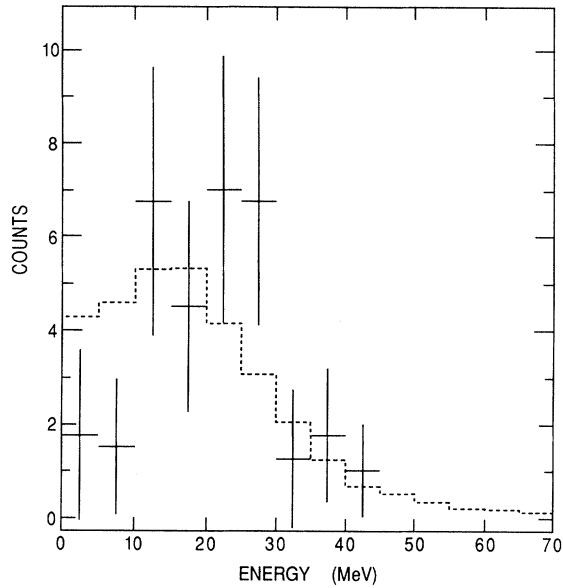
FIG. 22. Energy distribution for candidate decay-in-flight events. The energy distribution agrees with a Monte Carlo simulation (histogram).

F. Final-event sample

The remaining sample of beam-associated electrons contains a total of 56 beam-on and 65 beam-off events. After correcting for livetimes, the net excess is 38.5 ± 7.8 events. We attribute this excess to beam-stop neutrino interactions. We have shown that the events produced by beam-associated neutrons are negligible; the beam-associated neutron flux is small and the probability that a neutron induced event would pass our selection criteria is below 0.2%. In the next section we discuss the expected excess from conventional neutrino interactions. Tables III and IV summarize the trigger efficiencies and the analysis efficiencies for identifying events from $\bar{\nu}_e + p \rightarrow e^+ + n$.

IV. NEUTRINO CROSS SECTIONS AND SENSITIVITIES

The differential cross section for inverse beta decay can be expressed from first principles in terms of hadronic form factors [28]. Keeping only those terms of first order in momentum transfer, we have

$$\frac{d\sigma}{d\Omega}(\bar{\nu}_e + p \rightarrow e^+ + n)$$

$$= \frac{G^2 pE}{2\pi^2} \left[F_1^2 \cos^2\frac{\theta}{2} + F_A^2 \left[1 + \sin^2\frac{\theta}{2}\right] \right.$$

$$+ \frac{2F_A}{M} F_1(\mu_p + \mu_n) \left[Q + v^2 \sin^2\frac{\theta}{2}\right]^{1/2}$$

$$\left. \times \sin\frac{\theta}{2}\right], \tag{3}$$

where $G = 1.13 \times 10^{-5}/\text{GeV}^2$; p, E, and θ are the positron momentum, energy, and scattering angle; in units of nuclear magnetons, $\mu_p + \mu_n = 4.71$; Q^2 is the four-momentum-transfer squared; and $v = E_v - E$ for neutrino energy E_v. The form factors F_1 and F_A are known at $Q^2 = 0$: $F_1(0) = 1$ from the conserved-vector-current hypothesis and $F_A(0) = -1.262$ from measurements of neutron beta decay; the Q^2 dependence the form factors is ignorable for the low-energy neutrinos. Note, however, that the Q^2 dependence of the third term, which is a manifestation of "weak magnetism," decreases the total cross section by about 10% at the energies of this experiment.

The ν_μ and $\bar{\nu}_\mu$ from π^+ and μ^+ decaying at rest are below threshold for producing muons. However, a ν_e can have interactions with a complex nucleus can produce electrons in the detector. The detector composition is summarized in Table II. The most abundant isotopes are ^{12}C and ^{16}O, but these nuclei have small neutrino cross sections with high thresholds. The odd-A trace isotopes ^{13}C and ^{27}Al have much larger cross sections and lower thresholds. The contribution from the small amount of Gd in the detector is negligible.

TABLE IV. Data reduction for events in the beam-on gate and the beam-off gate. The data selection cuts are described in the text.

Cut	Beam on		Beam off	
	Events remaining	Relative reduction	Events remaining	Relative reduction
	549 168		2025 107	
In-time shield	397 489	0.724	1466 353	0.724
Track	229 673	0.578	852 574	0.581
Fiducial	119 131	0.519	437 366	0.513
Stopped muon	10 291	0.086	38 056	0.087
Particle identification	1 101	0.107	3 849	0.101
Associated energy	922	0.837	3 249	0.844
Shield veto	126	0.137	210	0.065
Total energy	110	0.873	138	0.657
Decay-in-flight/past hits	56	0.509	65	0.471

The neutrino cross sections for nuclei are generally difficult to calculate, especially when excited final states are considered. For ^{12}C and ^{16}O we use a computer program developed by Donnelly [29]. The program uses spherical shell model wavefunctions and calculates the full differential cross section. For the reaction ^{12}C $(v_e, e^-)^{12}N$ (g.s.), however, the cross section is simply related experimental lifetime for ^{12}N beta decay. The resulting neutrino cross section has been verified experimentally [30]. For ^{13}C and ^{27}Al we use the energy dependence and angular distributions obtained by Donnelly's method, but to account for Gamow-Teller quenching we renormalize the cross section to (p, n) reaction data [31], following the procedure of Fukugita *et al.* [32]. Based on comparisons with the available data, we assign an uncertainty of 5% to the ^{12}C ground-state cross section. For the other important reactions one must assess the reliability of the wave functions involved; we assign an error of 30% to ^{16}O and the ^{12}C excited state cross sections, and 50% to the ^{13}C and ^{27}Al cross sections that involve additional normalization uncertainties. Our experiment is also sensitive to electrons from elastic scattering of v_μ, $\bar{v}_\mu$, and v_e on electrons in the detector. The relevant elastic scattering cross sections are reliably calculated in the standard model since there are no hadronic matrix form factors involved and there is experimentally verification [33].

We use the Monte Carlo code to generate events from the expected neutrino interactions. For each neutrino energy, the number of events is weighted by the normalized cross section and the corresponding incident neutrino energy spectrum. For nuclear reactions the v_e energy spectrum is relevant, while for inverse beta-decay induced by $\bar{v}_e$, the appropriate neutrino energy spectrum distribution depends on which oscillation mode is being considered. Figure 23 displays the expected distributions of events
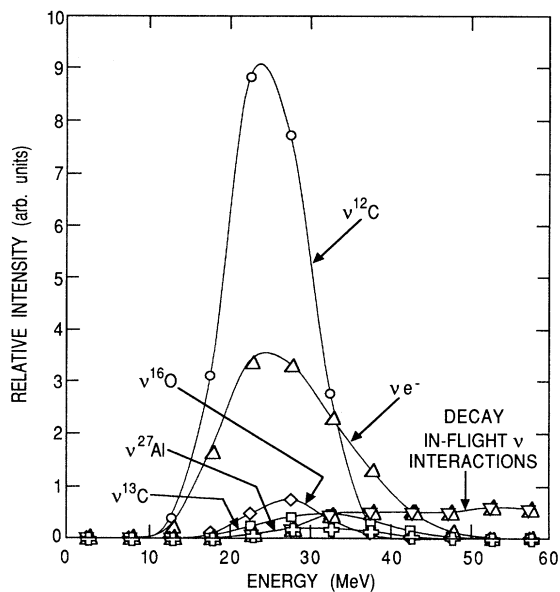
from the different background neutrino reactions. The largest contributions come from $v_e + {}^{12}$C and $v_e + e$ scattering.

The energy distribution of the final-event sample in Fig. 24 is shown separately for beam-on, beam-off, and the resulting beam excess. It is evident that the distribution agrees with the calculated backgrounds and the assumption of no neutrino oscillations. The observed angular distributions, shown in Fig. 25, are also consistent with this assumption. The ambiguity in the angle θ is resolved by choosing the smallest angle of the electron track relative to the incident neutrino direction. In the analysis shown in the figure, PDT drift time information, which improves the spatial resolutions to about 3 mm, has been employed. There is an additional ambiguity in the sign of the drift-time-implied displacement from the wire. To resolve this we adopt the following procedure. In each view we identify the track with the lowest χ^2 with respect to locations of the PDT hits. If there are only two hits in the view, we choose the combination that gives the smallest angle θ. To account for the introduced bias, the same procedure is used on Monte Carlo generated events. The spatial distribution of events in the detector, shown in Fig. 26, is consistent with the expected decrease with distance from the neutrino source. The observed distributions of the confidence level from the likelihood functions L_{SCI} and L_{PDT}, shown in Fig. 27, are flat, as expected for electrons.

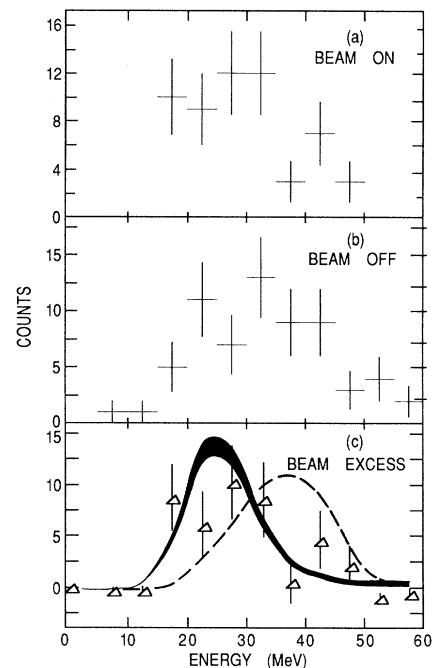FIG. 23. Expected energy distributions from background neutrino processes listed in Table V.

FIG. 24. Energy distribution for final event sample: (a) events in the beam-on gate, (b) beam-off gate (normalized by live time), and (c) beam excess. The shaded region indicates the distribution expected from nonoscillation neutrino processes. The dotted curve indicates the expected shape of a 5% $\bar{v}_\mu \rightarrow \bar{v}_e$ neutrino oscillation signal.
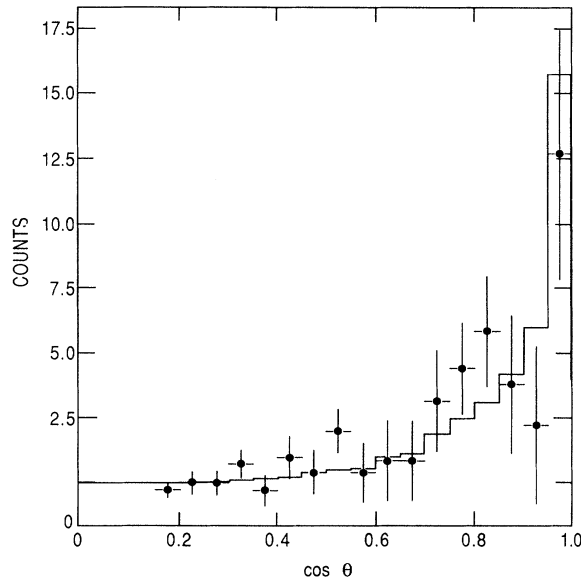
FIG. 25. The angular distribution of beam-excess events compared with a Monte Carlo simulation (histogram). The angle θ is measured with respect to an axis pointing from the beam stop to the track endpoint nearest the beam stop.

The relative sensitivities to the three oscillation modes and to the various background neutrino reactions are listed in Table V. The different average cross sections and trigger efficiencies for the three oscillation modes come from differences in the incident neutrino energies. Table V also contains the total number of events expected for the various neutrino reactions. For the purpose of comparison we have assumed complete transformation of the particular relevant neutrino species into $\bar{\nu}_e$. The calculat-
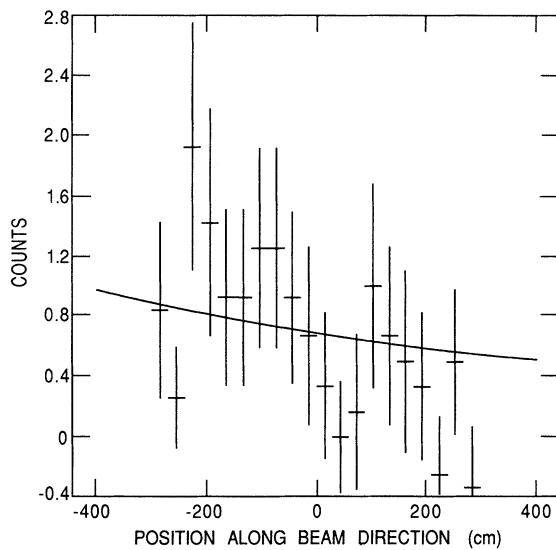

FIG. 26. Distribution of beam-excess event track centroids along the detector axis compared with a Monte Carlo simulation (solid line). Zero is the center of the detector.
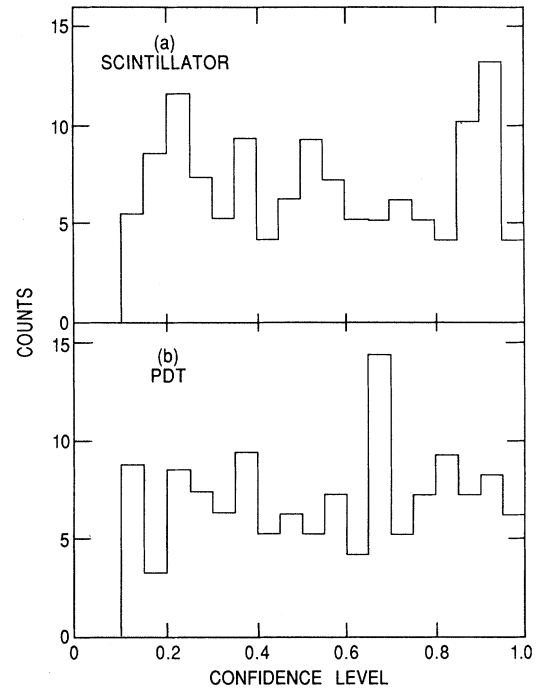

FIG. 27. Electron confidence level distributions for: (a) scintillation counters and (b) proportional drift tubes. These are the projections subsequent to the CL cut of Fig. 19. Electrons are expected to yield uniform distributions.

ed average flux for each type of neutrino is $8.32 \times 10^{13}/\text{cm}^2$ for the measured 26.6-m average source to detector distance, the total integrated beam current of 13 871 Coulombs, and the determined average number of π^+ decays per proton of 0.086. We would expect a total of 45.4 ± 4.3 beam-excess events with no neutrino oscillations, in agreement with our observed excess of 38.5 ± 7.8.

In the absence of neutrino oscillations, the data below 35 MeV in Fig. 24 can be used to determine the scale of $\nu_e + {}^{12}\text{C}$ cross section. The shape of the electron energy distribution from $\nu_e + {}^{12}\text{C}$ interactions is taken from the Monte Carlo result shown in Fig. 23. Correcting with the calculated number of events from elastic electron-neutrino scattering and neutrino scattering on ${}^{13}\text{C}$, ${}^{27}\text{Al}$, and ${}^{16}\text{O}$ and accounting for the propagated errors, we obtain a total neutrino-${}^{12}\text{C}$ cross section of $(0.103 \pm 0.043) \times 10^{-40}$ cm^{-2}. The errors are dominated by the statistics of the beam-on data below 35 MeV.

V. DATA ANALYSIS WITH NEUTRON DETECTION

Implementing neutron detection obviously reduces the detection efficiency, but the background neutrino reactions have essentially no neutrons in the final state, so the method promises improvements in the signal-to-background ratio. As we shall see, this analysis method yields a limit with similar significance when compared to the previous method. This analysis consists of two parts:

TABLE V. Neutrino reactions in the apparatus. Trigger and analysis efficiencies are calculated using the Monte Carlo program with the appropriate differential cross section and neutrino spectrum. The signal reactions assume total oscillation into $\bar{\nu}_e$.

Reaction	Flux averaged cross section $(10^{-41}\ cm^2)$	Number of targets $(\times 10^{+30})$	Trigger efficiency	Analysis efficiency	Expected number of events
Signals					
$\bar{\nu}_\mu \rightarrow \bar{\nu}_e$	9.60	1.51	0.250	0.305	925.0±83.0
$\nu_e \rightarrow \bar{\nu}_e$	7.43	1.51	0.205	0.306	587.0±55.0
$\nu_\mu \rightarrow \bar{\nu}_e$	6.24	1.51	0.125	0.299	295.0±30.0
Backgrounds					
$\nu_e + {}^{12}C \rightarrow e^- + X$	1.32	7.93×10^{-1}	0.085	0.303	22.7±2.9
$\nu_e + {}^{13}C \rightarrow e^- + X$	4.36	8.84×10^{-3}	0.191	0.308	1.9±1.0
$\nu_e + {}^{16}O \rightarrow e^- + X$	0.73	1.40×10^{-1}	0.065	0.311	1.7±0.5
$\nu_e + {}^{27}Al \rightarrow e^- + X$	2.90	6.35×10^{-3}	0.137	0.316	0.7±0.3
$\nu + e \rightarrow \nu + e$	0.040	7.44	0.159	0.325	12.9±1.3
Decay-in-flight					5.5±2.3
Total neutrino background					45.4±4.3

the selection of the neutrino candidates; and the testing of these candidates for a delayed neutron capture signal. The analysis is performed on a slightly different data set consisting of 2.48×10^6 raw events. The integrated proton charge on the beam dump is 12 913 Coulombs.

A. Selection of neutrino candidates

The neutrino candidates are selected by using background removal techniques that are similar to those described above. The details of the selection criteria are found in Ref. [22]. The neutrino selection results in 72 beam-on and 106 beam-off events and the beam excess is 43.8±8.9 events. The selection efficiency is estimated from Monte Carlo calculations to be 34.1% for $\bar{\nu}_\mu$ oscillating into $\bar{\nu}_e$. The Monte Carlo calculations also predict a beam excess of 49.0±5.0 events from background neutrino reactions, in good agreement with the observed beam excess.

B. The neutron signal

Neutrons are detected by observing the gamma rays from radiative neutron capture on Gd. The neutrino candidate events are scrutinized for evidence of neutron capture signals in delayed coincidence with the electron. In order to reduce the accidental coincidence rate, we impose conditions of the neutron capture signal that should not be satisfied by potential backgrounds. In this case, the largest background is from ambient radioactivity. Since neutron capture on Gd emits on average about four gamma rays with a total energy of about 8 MeV, the signature is specified by two or more coincident hits in scintillators within 150 cm of the detected electron track and with at least one of the scintillator counters having detectable signals from both PMTs. In addition, the visible energy from the delayed capture signal must be less than 9 MeV. We define the coincidence window for the detection of the Gd capture photons to be from 5 to 110 μs subsequent to the electron being detected. Monte Car-

lo simulations using this specified signature yield a neutron detection efficiency in agreement with our observations using the spontaneous fission ^{252}Cf source. The neutron detection efficiency for the process $\bar{\nu}_e + p \rightarrow e^+ + n$ will be slightly different because of differences in energy and spatial distributions. To determine the overall efficiency and the background of delayed neutron capture signals, we rely upon Monte Carlo generated data that is superimposed upon data obtained with the detector randomly triggered. The efficiency for detecting the neutron signature is 32.5% for neutrons from $\bar{\nu}_e + p \rightarrow e^+ + n$. The accidental probability that a background neutrino reaction will have a delayed signal simulating the neutron capture signature is 10.6%.

Processing the events with candidate neutrino-induced electron signals we find 11 beam-on and 10 beam-off events have delayed neutron capture signals. This corresponds to a beam excess of 8.3±3.4 events. We expect 334.4±26.7 events for complete $\bar{\nu}_\mu$ oscillations. The predicted background is 5.2±0.5 events from accidental coincidences.

C. Removal of background neutrino events

The beam excess contains a signal component S, from $\bar{\nu}_e + p \rightarrow e^+ + n$, and a background component B. It is evident from the previous analysis that B consists primarily of events induced by the background neutrino interactions; we take this as an assumption in the present analysis. The neutrino candidates can be divided into a set X if they are in coincidence with neutron signals and a set Y if they are not. In terms of S and B, we have:

$$X = \varepsilon S + rB \quad \text{and} \quad Y = (1 - \varepsilon)S + (1 - r)B ,$$

where ε is the neutron detection efficiency and r is the accidental probability. These two simultaneous equations (with and without neutron observation) can be solved simultaneously for the signal S. Thus the present analysis is independent of the exact form of the background neutrino interactions.

VI. RESULTS

We begin by discussing the conclusions of the analysis that does not invoke neutron detection. The final data sample displayed in Fig. 24 is used to deduce 90% confidence level (90% CL) upper limits on neutrino flavor oscillations $\bar{v}_\mu \rightarrow \bar{v}_e$, and the Majorana oscillation modes $v_e \rightarrow \bar{v}_e$ and $v_\mu \rightarrow \bar{v}_e$. The experiment can be used to set limits on direct $\bar{v}_e$ production, and we shall obtain a constraint on the lepton number violating process $\mu^+ \rightarrow e^+ + \bar{v}_e + v_\mu$. Most of the previous accelerator-based neutrino oscillation experiments used beams of high energy v_μ, but not $\bar{v}_\mu$.

We obtain the limits on the various oscillation modes using a maximum likelihood analysis. We also perform the corresponding analyses using χ^2 and a Bayesian method [34], obtaining similar limits. The likelihood calculation accounts for the Poisson statistics in the number of beam-on and beam-off events that are partitioned into 5-MeV-wide energy bins. For each of the various neutrino processes we use the appropriate cross section with the uncertainties discussed in Sec. IV. The Monte Carlo code provides the detector acceptances and the finite-energy resolution distortion for each. An 8% systematic error is assigned to the neutrino flux, coming primarily from the uncertainty in the π^+ decay to proton ratio. The triggering efficiency and the efficiency of the event selection procedures are summarized in Table III. The analysis is found to be relatively insensitive to reasonable variations of these systematic uncertainties. The stringency of the experimental upper limits are statistics limited by the number of events in the beam-on gate.

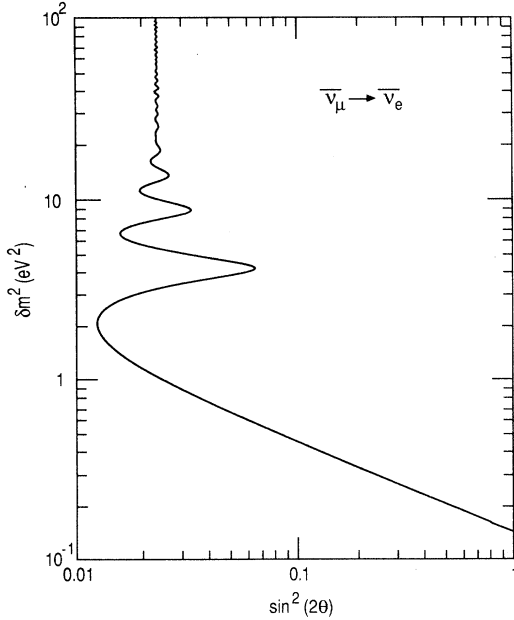For the neutrino flavor oscillation mode, $\bar{v}_\mu \rightarrow \bar{v}_e$, we
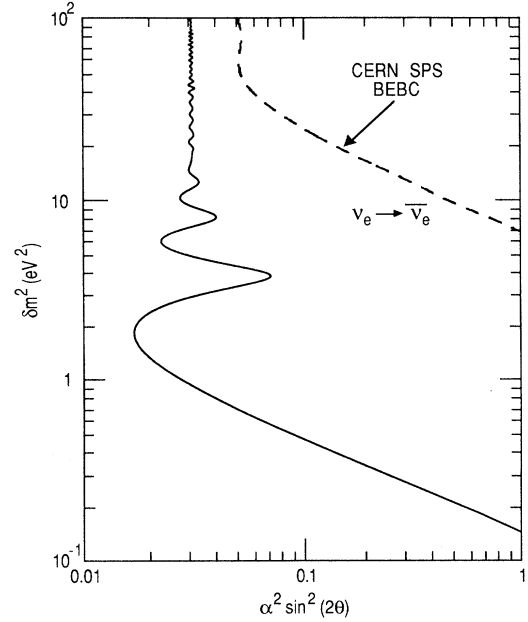

FIG. 29. The 90% confidence level contour for the region of δm^2 and $\alpha^2 \sin^2(2\theta)$ excluded by this experiment for $v_e \rightarrow \bar{v}_e$ oscillations (solid curve). The dotted curve is from Ref. [14].

obtain the following (90% CL) limits:

$$\delta m^2 < 0.14 \text{ eV}^2, \quad \text{for maximal mixing},$$

$$\sin^2(2\theta) < 0.024, \quad \text{for large } \delta m^2.$$
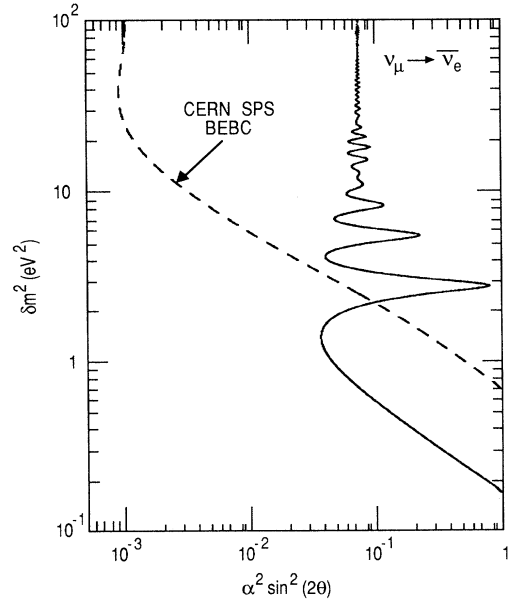
Figure 28 shows the 90% CL contour for the region of

FIG. 28. The 90% confidence level contour for the region of δm^2 and $\sin^2(2\theta)$ excluded by this experiment for $\bar{v}_\mu \rightarrow \bar{v}_e$ oscillations.

FIG. 30. The 90% confidence level contour for the region of δm^2 and $\alpha^2 \sin^2(2\theta)$ excluded by this experiment for $v_\mu \rightarrow \bar{v}_e$ oscillations (solid curve). The dotted curve is from Ref. [14].
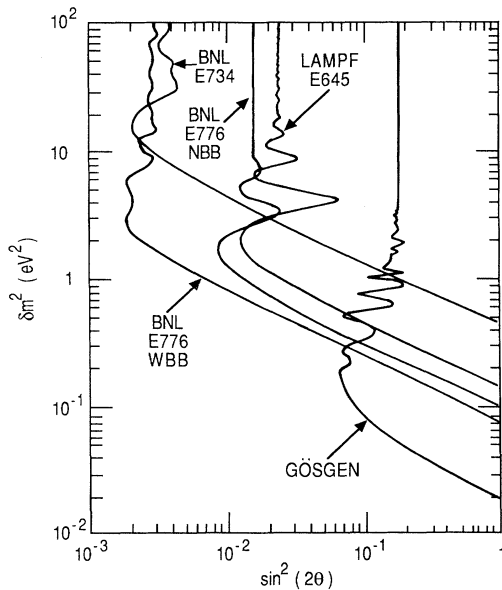
FIG. 31. Comparison of selected flavor-changing neutrino oscillation limits. The figure combines limits from appearance experiments with neutrinos and antineutrinos with the best limits from reactor disappearance experiments. The limits are comparable under the simplest assumptions of two-flavor neutrino mixing. See (Blumenfeld *et al.*) Ref. [10], BNL 776 NNB (narrow band beam); (Borokovsky *et al.*) Ref. [10], BNL WBB (wide-band beam); (Ahrens *et al.*) Ref. [9], BNL E734; and (Zacek, *et al.*), Ref. [6], Gösgen.

oscillation parameters excluded by this experiment. The limits presented here are slightly worse than our previously reported limits [17] that are based on a smaller data sample. We attribute this to a downward statistical fluctuation in the early data, that did not persist as additional data was collected. The present analysis is also based on a more precise model of the detector.

For the Majorana neutrino oscillation model, $v_e \rightarrow \bar{v}_e$, we have

$$\delta m^2 < 0.14 \text{ eV}^2, \quad \text{for maximal mixing},$$

$$\alpha^2 \sin^2 2\theta < 0.032, \quad \text{for large } \delta m^2$$

at the 90% CL. The interpretations of the parameter δm^2 and $\sin^2 2\theta$ for this mode are discussed in Refs. [13,35]; the quantity α parameterizes the mixture of

right-handed currents in the hypothetical theory. Figure 29 shows the 90% CL contours for the excluded region.

Additionally, for the neutrino oscillation process $v_\mu \rightarrow \bar{v}_e$ we have the following 90% CL limits:

$$\delta m^2 < 0.16 \text{ eV}^2, \quad \text{for maximal mixing},$$

$$\alpha^2 \sin^2 2\theta < 0.072, \quad \text{for large } \delta m^2.$$

Figure 30 shows the exclusion contours.

The 90% CL limit is 0.012 for the fraction of μ^+s that could have decayed by the lepton-number-violating process $\mu^+ \rightarrow e^+ \bar{v}_e v_\mu$. As expected the limit corresponds to about on-half the large δm^2 limit on flavor oscillations channel, $\bar{v}_\mu \rightarrow \bar{v}_e$. Another experiment recently reported a 90% Cl upper limit of 0.018 on the same process [36].

The limits from the analysis with a neutron signature are slightly less stringent, but they provide useful confirmation. For flavor oscillations, for example, they give a large δm^2 limit of $\sin^2 2\theta < 0.034$ (90% CL). We emphasize, however that this limit is independent of the energy distribution of the background from beam neutrinos.

In conclusion, we have performed a neutrino oscillation search using neutrinos from π^+ and μ^+ decaying at rest. The backgrounds are well understood and the detector has been carefully calibrated using electrons from decays of stopped muons. We find no evidence for neutrino oscillations. Our results for the most common scenario of two-flavor mixing is compared with other experiments in Fig. 31.

[1] W. Marciano, in *Intersections Between Particle and Nuclear Physics*, Proceedings of the 3rd Conference, Rockport, Maine, 1988, edited by Gerry M. Bunce, AIP Conf. Proc. No. 176 (AIP, New York, 1988), p. 193; P. Langacker, in *Massive Neutrinos:* Proceedings of an International Workshop, Heidelberg, West Germany, 1987, edited by H. V. Klapdor and B. Povh (Springer-Verlag, Berlin, 1988).

[2] R. G. H. Robertson *et al.*, Phys. Rev. Lett. **67**, 957 (1991); R. G. H. Robertson and D. A. Knapp, Annu. Rev. Nucl. Part. Sci. **38**, 185 (1988).

[3] R. D. Bolten *et al.*, Phys. Rev. D **38**, 2077 (1988).

[4] B. Pontecorvo, Zh. Eksp. Teor. Fiz. **33**, 549 (1957) [Sov. Phys. JETP **6**, 429 (1958)]; **53**, 1717 (1967) [**26**, 984 (1968)]; Z. Maki *et al.*, Prog. Theor. Phys. **28**, 870 (1962); S. M. Bilenky and B. Pontecorvo, Phys. Rep. **41C**, 225 (1978).

[5] Some recent reviews of neutrino oscillation experiments include the following: S. M. Bilenkii and S. T. Petcov, Rev. Mod. Phys. **59**, 671 (1987); **61**, 169 (1989); V. Flaminio and B. Saitta, Riv. Nuovo Cimento **10**(8), 1 (1987); F. Boehm, Nucl. Instrum. Methods A **264**, 114 (1988).

[6] G. Zacek *et al.*, Phys. Rev. D **34**, 2621 (1986); A. I. Afonin *et al.*, Pis'ma Zh. Eksp. Teor. Fiz. **42**, 230 (1985) [JETP Lett. **42**, 285 (1985)]; J. F. Cavaignac *et al.*, Phys. Lett. **148B**, 387 (1984).

[7] F. Bergsma *et al.*, Z. Phys. C **40**, 171 (1988); F. Dydak *et al.*, Phys. Lett. **134B**, 281 (1984); I. E. Stockdale *et al.*, Phys. Rev. Lett. **52**, 1384 (1984); F. Bergsma *et al.*, Phys. Lett. **142B**, 103 (1984); S. V. Belikov *et al.*, Pis'ma Zh. Eksp. Teor. Fiz. **38**, 547 (1983) [JETP Lett. **38**, 661 (1983)].

[8] P. Astier *et al.*, Nucl. Phys. **B335**, 517 (1990); P. Astier *et al.*, Phys. Lett. B **220**, 646 (1989); T. Dombeck *et al.*, *ibid.* **194**, 591 (1987); G. Bernardi *et al.*, *ibid.* **181**, 173 (1986); G. N. Taylor *et al.*, Phys. Rev. D **28**, 2705 (1983); N. J. Baker *et al.*, Phys. Rev. Lett. **47**, 1576 (1981); J. Blietschau *et al.*, Nucl. Phys. **B133**, 205 (1978); G. Danby *et al.*, Phys. Rev. Lett. **9**, 36 (1962).

[9] L. A. Ahrens *et al.*, Phys. Rev. D **31**, 2732 (1985).

[10] B. Blumenfeld *et al.*, Phys. Rev. Lett. **62**, 2237 (1989); L. Borokovsky *et al.*, *ibid* **68**, 274 (1992).

[11] C. Angelini *et al.*, Phys. Lett. B **179**, 307 (1986).

[12] N. Ushida *et al.*, Phys. Rev. Lett. **57**, 2897 (1986); E. Dydak *et al.*, Phys Lett. **134B**, 281 (1984).

[13] J. N. Bahcall and H. Primakoff, Phys. Rev. D **18**, 3463 (1978).

[14] A. M. Cooper *et al.*, Phys. Lett. **112B**, 97 (1982).

[15] R. Davis, Phys. Rev. **97**, 766 (1955).

[16] G. V. Domogatskii, Yad. Fiz. **22**, 1265 (1975) [Sov. J. Nucl. Phys. **22**, 657 (1975)].

[17] L. S. Durkin *et al.*, Phys. Rev. Lett. **61**, 1811 (1988).

[18] R. C. Allen *et al.*, Nucl. Instrum. Methods A **284**, 347 (1989).

[19] B. Burman *et al.*, Nucl. Instrum. Methods A **291**, 621 (1990).

[20] L. S. Durkin *et al.*, Nucl. Instrum. Methods A **277**, 386 (1989).

[21] J. Napolitano *et al.*, Nucl. Instrum. Methods A **274**, 152 (1989).

[22] B. K. Fujikawa, Ph.D. thesis, California Institute of Technology, 1990; Los Alamos National Laboratory Report LA-11721-T (unpublished); J. W. Mitchell, Ph.D. thesis, The Ohio State University, 1989; Los Alamos National Laboratory Report LA-11539-T (unpublished); W. C. Choi, Ph.D. thesis, Louisiana State University, 1987; M. Timko, Ph.D. thesis, The Ohio State University, 1987.

[23] Neutrino Facility, LAMPF Users Handbook, LAMPF Report No. M-DO-3-UHB, Rev. 1984 (unpublished).

[24] R. L. Burman and E. S. Smith, " Parameterization of Pion Production and Reaction Cross Sections at LAMPF Energies," Los Alamos National Laboratory Report No. LA-1502-MS, 1988 (unpublished).

[25] Walter R. Nelson, Hideo Hirayama, and David W. O. Rogers, SLAC-Report-265, 1985 (unpublished).

[26] D. I. Garber and R. R. Kinsey, "Neutron Cross Sections, Volume II, Curves," BNL Report No. BNL-325, 1976 (unpublished), and references therein.

[27] J. S. O'Connell, in Proceedings of the Los Alamos Neutrino Workshop, p. 37; Los Alamos National Laboratory Report No. LA-9358-C, 1986 (unpublished); T. K. Gaisser and J. S. O'Connell, Phys. Rev. D **34**, 822 (1986).

[28] T. K. Gaisser and J. S. O'Connell, Phys. Rev. D **34**, 822 (1986).

[29] T. W. Donnelly (private communication); see also D. Krakauer, Ph.D. thesis, University of Maryland, 1989; Los Alamos National Laboratory Report No. LA-12262-T (unpublished).

[30] R. C. Allen *et al.*, Phys. Rev. Lett. **64**, 1871 (1990); D. A. Krakauer *et al.*, Phys. Rev. C **45**, 2450 (1992); B. Bodmann *et al.*, Phys. Lett. B **280**, 198 (1992).

[31] T. N. Tadeucci *et al.*, Nucl. Phys. **A469**, 125 (1987).

[32] M. Fukugita *et al.*, Phys. Rev. C **41**, 1359 (1990).

[33] R. C. Allen *et al.*, Phys. Rev. Lett. **64**, 1330 (1990).

[34] H. B. Prosper, Phys. Rev. D **37**, 1153 (1988).

[35] Henry Primakoff and S. Peter Rosen, Annu. Rev. Nucl. Part. Sci. **31**, 145 (1981).

[36] D. A. Krakauer *et al.*, Phys. Lett. B **263**, 534 (1991).